Digital image reduction for analysis of topological changes in pore space during chemical dissolution*

Dmitriy Prokhorov[0000−0002−8547−930X], Vadim Lisitsa[0000−0003−3544−4878], and Yaroslav Bazaikin[0000−0003−3043−4224]

Sobolev Institute of Mathematics SB RAS, 4 Koptug ave., Novosibirsk, Russia, 630090

Abstract. The paper presents an original algorithm for reducing three-dimensional digital images to improve persistence diagrams computing performance. These diagrams represent topology changes in digital rocks pore space. The algorithm has linear complexity because removing the voxel is based on the structure of its neighborhood. We illustrate that the algorithm's efficiency depends heavily on the pore space's complexity and the size of the filtration steps.

Keywords: Persistence homology · Digital image reduction · Chemical dissolution.

1 Introduction

Green energy and environmental geotechnologies such as CO_2 sequestration [15], and geothermal exploration [3], [12], [17] rises new challenges in reservoir studies. In particular, reactive fluid transport and changes in the pore space geometry and topology due to chemical fluid-solid interaction become the dominant factor of the macroscopic properties (elastic stiffness, electric conductivity, seismic velocities, hydraulic permeability) changes of the aquifers [25], [13], [14], [2]. However, theoretical investigations and numerical simulations of the reactive transport are based on the reservoir-scale models of poromechanics, transport in porous media and coupled modems [26], [4], [29], [22]. These models use empirical relations between porosity, pore space geometry and topology, permeability, tortuosity, elastic stiffness, and others [26].

In recent years, a number of papers were published on experimental [15], [2], and numerical study [23], [11], [27] of carbonates dissolution due to the reactive fluid injection. These experiments show that changes in the pore space geometry due to the rock matrix's chemical dissolution strongly depend on the reaction rate, flow rate, and mineral heterogeneity, resulting in the various scenarios of

* The research is supported by the Russian Science Foundation grant no. 21-71-20003. Numerical simulations were performed using "Polytechnic RSC Tornado" (SPBSTU, Russia).

ICCS Camera Ready Version 2021
To cite this paper please use the final published version:
DOI: 10.1007/978-3-030-77961-0_32

macroscopic properties changes [2], [16]. Recently we presented the research on estimation of the pore space topology changes in 2D case, where the topology is characterized by three Betti numbers representing the number of the connected components of pore space (isolated pores), number of the connected components of the matrix, and the Euler number [16]. We also showed that the evolution of the pore space topology is related to the changes in the physical properties of rock samples. Thus, it can be used to measure pore space changes. In the 3D case, the Betti 1 number, representing the number of channels in the pore space, has the main effect on the rocks' transport properties. However, calculation of the cycles and their evolution requires numerically intense algorithms.

The dynamics of rock matrix dissolution can be expressed as a set of sequential digital images of rock. The sequence corresponds to discrete time, and each digital image represents a spatial sampling of the rock, for example, a tomographic image. In computational topology, such sequence (if it is monotonous) is called filtration, and the natural thought is to count topological filtration invariants called persistent Betty numbers. One of the advantages of persistent Betty numbers is that they evaluate the filtration's topological complexity (i.e., the number of relative homological cycles taken relative to the filtration level). Another property that is very important for applications is their stability with respect to filtration perturbation. It means that a small error in the data leads to a small error in the persistent diagram (the persistent diagram contains all the necessary information about persistent Betty numbers).

There are 0, 1, and 2-dimensional non-zero Betti numbers in three-dimensional space. Moreover, the calculation of 0 and 2-dimensional Betti numbers (number of isolated pores and number of isolated matrix components) are based on disjoint-set-union data structure [8], and the duality of digital spaces does not require high computational resources. A completely different situation is with one-dimensional ones; they can be calculated by the Edelsbrunner-Lettsher-Zomorodyan algorithm, which has cubic complexity from the image size [8].

The paper's main idea is to use the image reduction algorithm compatible with the Edelsbrunner-Letscher-Zomorodyan algorithm for calculating persistent diagrams. We carried out a comparative test on rock samples obtained by statistical modeling methods, in particular by truncated Gaussian field method [10], and on real dissolved samples [2], [1]. It is shown that the reduction algorithm makes it possible to accelerate the calculation of persistent Betty numbers. However, the acceleration depends on the porosity, correlation length of the samples, and the discrete time step's size.

2 Digital images

Let us define a regular spatial grid with points $p_I = (x_{i_1+\frac{1}{2}}, y_{i_2+\frac{1}{2}}, z_{i_3+\frac{1}{2}})$, where $I \in N^3$, and $x_{i_1+\frac{1}{2}} = h_x(i_1 + \frac{1}{2})$, $y_{i_2+\frac{1}{2}} = h_y(i_2 + \frac{1}{2})$, $z_{i_3+\frac{1}{2}} = h_z(i_3 + \frac{1}{2})$, with h_x, h_y, and h_z are the grid steps. Note, that we are interested in the topology of the digital images, thus, we may state $h_x = h_y = h_z = 1$. Now, we can introduce the grid cell or voxel as $C_I = \{(x, y, z) \in R^3 | i_1 \leq x \leq i_1 + 1, i_2 \leq y \leq i_2 + 1, i_3 \leq$

ICCS Camera Ready Version 2021
To cite this paper please use the final published version:
DOI: 10.1007/978-3-030-77961-0_32

$z \leq i_3 + 1\}$. Using these notations the segmented digital image can be defined as a piece-wise constant function $F(x, y, z)$ mapping rectangular spatial domain $D \subseteq R^3$ to a finite subset of integer numbers $A = \{0, 1, ..., M\}$. A natural choice for the digital rock physics applications is a binary image; i.e., $A = \{0, 1\}$, where 0 corresponds to the *background* and 1 represents the *foreground*. In particular, if fluid flow [5], [6] or electric current in porous space is studied, 1 represents pore space and 0 corresponds to the rock matrix.

The set of voxels $X = \cup_{I=1}^{N} C_I$, so that $F(\boldsymbol{x} \in X) = const$, forms a topological space $X(X, T)$ if the topology T is introduced. The topology T on X can be defined in several ways [8]. In particular, we deal with *6-neighborhood rule*; that is the voxels are neighbors if they share a face, and *26-neighborhood rule*; that is the voxels are neighbors if they share either a face, or an edge, or a vertex. $X = (X, T)$ is called a digital image's topological space or a three-dimensional digital image.

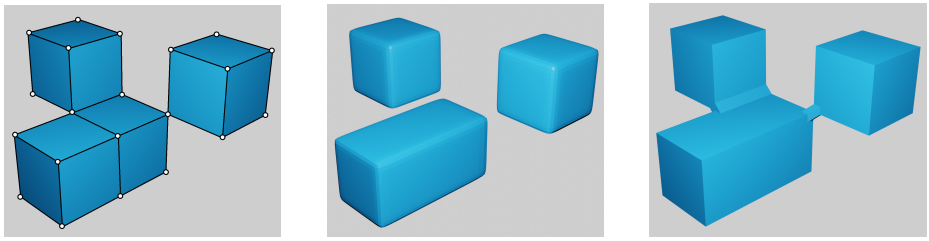

Fig. 1. A fragment of a digital image and its topological implementation for cases of 6- and 26-neighborhood rule

In numerical modeling, space's topology is indirectly defined by choice of the numerical method. In particular, if the fluid flow is simulated using the finite-difference or finite-volume method, the topology of the pore space corresponds to the 6-neighborhood rule because flows are determined through the cells' faces [16], [9]. Therefore, the voxels included in the complement (rock matrix) has 26-neighborhood rule; thus, advanced numerical approximations such as rotated grids [24], or finite-elements on hexagonal grids should be utilized if coupled problems are solved [21], [18].

Let us consider sequence of digital images with the following topological spaces $\{X_i\}_0^m$ such as $\emptyset = X_0 \subseteq X_1 \subseteq X_2 \subseteq ... \subseteq X_m = X$, and call this sequence *filtration*. Filtration of a binary image can also be presented as an artificial multi-component digital image:

$$F(\boldsymbol{x}) = \begin{cases} 0, \boldsymbol{x} \in \text{background of } X \\ k, \boldsymbol{x} \in X_k \backslash X_{k-1} \end{cases} \quad (1)$$

ICCS Camera Ready Version 2021
To cite this paper please use the final published version:
DOI: 10.1007/978-3-030-77961-0_32

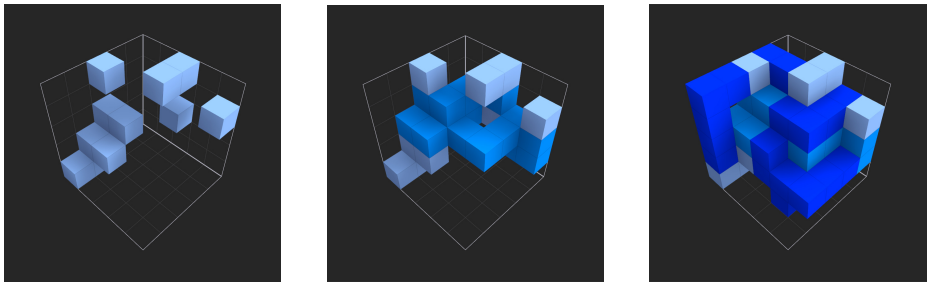

Fig. 2. Filtration of the binary image $X_0 \subseteq X_1 \subseteq X_2$, where voxels from

For each pair of indices $0 \leq i < j \leq m$, the embedding $X_i \subseteq X_j$ induces a homomorphism of p-dimensional homology groups (we consider cellular homology with coefficients in Z_2):

$$f_p^{i,j} : H_p(X_i) \to H_p(X_j). \tag{2}$$

The p-dimensional persistent homology group is the image of the homomorphism considered above: $H_p^{i,j} = Im(f_p^{i,j})$. The rank of this group $\beta_p^{i,j}$ is called *p-dimensional persistent Betty number.*

3 Edelsbrunner algorithm

The Edelsbrunner-Lettsher-Zomorodyan algorithm [8] is a common way to calculate persistent Betty numbers. The original implementation is described for simplicial complexes. A *k-simplex* σ is the convex hull of $k+1$ affinely independent points $S = \{v_0, v_1, ..., v_k\}$. A simplex τ defined by $T \subseteq S$ is a face of σ. And a *simplicial complex* is finite set of simplices such that

1. $\sigma \in K$, τ is a face of $\sigma \Rightarrow \tau \in K$
2. $\sigma, \tau \in K \Rightarrow \sigma \cap \tau$ is a face of σ and face of τ

The nested sequence of simplicial complexes $\emptyset = K_0 \subseteq K_1 \subseteq K_2 \subseteq ... \subseteq K_m = K$ is *filtration.*

Therefore, the first task that arises in calculating persistent homologies of a digital image is the triangulation of the image and the definition of filtration on the resulting complex. It is worth noting that triangulation is not required, because cubic homology is equivalent to simplicial. So the image can be converted to *unit cubic complex*, which is more natural. It is defined in the same way as simplicial, but instead of k-simplexes cubical complex consists of k -dimensional unit cubes.

Thus, in the case of the 26-neighborhood rule, each voxel can be considered a three-dimensional unit cube. Moreover, in the case of the 6-neighborhood rule, it is convenient to use the more efficient approach described in [28].

ICCS Camera Ready Version 2021
To cite this paper please use the final published version:
DOI: 10.1007/978-3-030-77961-0_32

Here is a description of the Edelsbrunner-Lettsher-Zomorodyan algorithm. Let all the simplexes in the complex are numbered according to the filtration [8]. It means that

1. If σ_{i_1} is a face of σ_{i_2} then $i_1 \leq i_2$.
2. If $\sigma_{i_1} \in K_i$ and $\sigma_{i_2} \in K_{i+j} \backslash K_i$ for $j > 0$ then $i_1 \leq i_2$

We have a sequence of simplices $\sigma_1, \sigma_2, ..., \sigma_n$. The data is stored in a linear array $R[1..n]$, whose elements are lists of simplexes.

Algorithm 1 Edelsbrunner-Lettsher-Zomorodyan algorithm

```
1: for j ← 1 to m do
2:     L ← list of faces of the σ_j
3:     R[j] ← NULL
4:     while L ≠ NULL and R[i] ≠ NULL, where i is the largest number of simplices
       in L do
5:         L ← L △ R[i]
6:     end while
7:     if L ≠ NULL then
8:         R[i] ← L
9:     end if
10: end for
```

The fulfillment of the last condition gives the following information - a cycle born at time i is destroyed at time j. Moreover, the failure corresponds to the birth of the cycle at the time of j. Iterations of the inner while loop are called *collisions*. They take most of the running time of the algorithm.

Consider an example in which σ_k and σ_{k+1} are triangles and σ_{k-5}, ..., σ_{k-1} are their edges, where σ_{k-1} is common. And let these simplices belong to $K_l \backslash K_{l-1}$. Collisions occur when σ_{k-2} and σ_{k-1} are added. It means the birth of one-dimensional cycles. These cycles die when σ_k and σ_{k+1} are added. Since all these simplexes belong to one filtration step, they are not considered in the final result. There can be many collisions in large complexes, including cubic ones that do not carry information about persistent homology groups. Therefore, the question arises. Is it possible to reduce their number? The answer to this question is positive; one way is to remove the corresponding simplexes.

4 Reduction algorithm

The reduction algorithms for simplicial and cubic complexes based on retraction are quite simple. Their main idea is the sequential removal of free faces, which means a retraction of simplexes (cubes). More efficient co-reduction algorithms are also known now [19]. Among other things, they are used for calculating persistent homologies [20].

ICCS Camera Ready Version 2021
To cite this paper please use the final published version:
DOI: 10.1007/978-3-030-77961-0_32

This part of the paper describes an algorithm based on retraction. The version of the algorithm described in [7] adapted for 3-d digital images with the 6-neighborhood rule.

The algorithm takes the digital image representing filtration $\{X_i\}_0^n$ as an input. After that, it sequentially removes voxels according to rules described below, beginning with voxels that have value n and down to 1.

1. All conditions are checked in voxel neighborhood of size $3 \times 3 \times 3$.
2. Number of connected components of the foreground of X_n with and without current voxel is the same.
3. Number of connected components of the background of X_n is equal to 1.
4. Euler characteristic of the foreground of X_n with and without current voxel is the same.
5. Current voxel is not in any parallelepiped consisted of foreground of X_n with size $1 \times 1 \times 2$ or $1 \times 2 \times 2$ or $2 \times 2 \times 2$ that contains voxels with greater value.

If the voxel is removed, its value becomes equal to 0, and the algorithm rechecks his neighbors.

It is easy to show that the reduction algorithm has linear complexity of the number of voxels in the image. Checking the rule has a constant running time. Moreover, each voxel is checked no more than seven times because it has only six neighbors.

5 Numerical experiments

5.1 Statistical models

In the first series of experiments, the algorithm was applied to filtration obtained by "uniform" dissolution of the rock described in [16]. Here was assumed that the reagent concentration is constant, which leads to the same speed of movement of the pore space – rock matrix interface. The original images were obtained by the truncated Gaussian field method [10]. The main parameters in image generation were porosity and correlation length. The size of individual pores in the image depends on the correlation length.

We generated 160 samples of the size 250^3 voxels. We considered the porosity varied from 0.05 to 0.2 with the increment of 0.05, and the correlation length varied from 5 to 20 voxels with the step of 5. Thus, for each pair of parameters (porosity, correlation length), ten statistical realizations were generated. The simulation process had 100 time steps for all samples.

For all of these images, 1-dimensional barcodes were calculated before and after reduction. In each experiment, they were equal up to permutation. This fact confirms the correctness of the implementation of the algorithm.

The time of 1-dimensional barcodes computation was also measured. The figure 3 shows the acceleration coefficient averaged by the samples' parameters. It is important to note that the acceleration coefficient was calculated without

ICCS Camera Ready Version 2021
To cite this paper please use the final published version:
DOI: 10.1007/978-3-030-77961-0_32

taking into account the time spent on reduction. It is because the Edelsbrunner-Lettsher-Zomorodyan algorithm has cubic complexity, and the reduction algorithm is linear. Therefore the time spent on reduction becomes insignificant when image size is increasing.

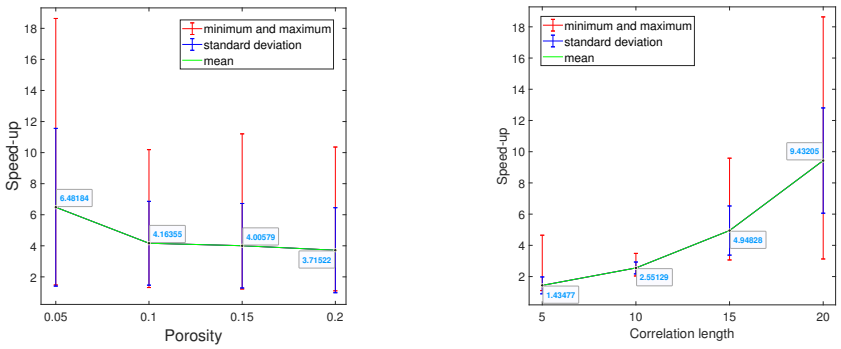

Fig. 3. The average value of the acceleration of the calculation of persistent Betty numbers depending on porosity (left) and correlation length (right)

The graphs show that the highest acceleration was achieved for samples with low porosity and high correlation length. It is because the samples with larger surface area dissolve faster and form more complex topological structure. Averaging within each group of samples also confirms this assumption.

Table 1. The average acceleration of the algorithm depending on the porosity and correlation length

l;ρ	0.05	0.1	0.15	0.2
5	1.9	1.4	1.3	1.2
10	3.1	2.5	2.4	2.2
15	6.9	5.1	4.3	3.5
20	14.0	7.7	8.0	8.0

Table 2. The standard deviation of the algorithm acceleration depending on the porosity and correlation length

l;ρ	0.05	0.1	0.15	0.2
5	0.98	0.06	0.06	0.09
10	0.31	0.18	0.09	0.10
15	1.58	0.88	0.38	0.22
20	2.83	2.08	1.66	1.63

ICCS Camera Ready Version 2021
To cite this paper please use the final published version:
DOI: 10.1007/978-3-030-77961-0_32

Table 3. Maximum algorithm acceleration depending on porosity and correlation length

l;ρ	0.05	0.1	0.15	0.2
5	4.6	1.5	1.4	1.3
10	3.5	2.8	2.5	2.3
15	9.6	6.5	4.9	3.8
20	18.6	10.2	11.2	10.4

Table 4. Minimum algorithm acceleration depending on porosity and correlation length

l;ρ	0.05	0.1	0.15	0.2
5	1.5	1.3	1.2	1.1
10	2.5	2.2	2.2	2.0
15	4.7	3.9	3.8	3.0
20	10.8	3.1	6.0	5.9

5.2 Pore-scale dissolution by CO_2 saturated brine in a multi-mineral carbonate at reservoir conditions

The significant difference between these tests is that they were done on real images obtained as a result of the dissolution described in [1]. Here we present only the characteristics of the images. The original images had a size of 1000^3 with a voxel length of 5.2 μm and corresponded to heterogeneous rock samples consisting of 86.6% of dolomite and 11.1% of calcite. Ten images were showing the dynamics of dissolution for each experiment.

Filtration was obtained from these images assuming that pore space voxels do not become rock voxels at the later steps. Fragment of size $400 \times 340 \times 400$ was cut out from sample AH, and of size $260 \times 320 \times 400$ from AL because the main part of the pore space is located where fluid forms the channel.

Table 5. The results of the algorithm for calculating persistent Betty numbers with and without reduction

Sample	AH	AL
ELZ time. sec.	2485	445
Reduction time. sec.	240	101
ELZ time after reduction. sec.	35	15
Acceleration	71	29.67
Total acceleration	9.04	3.84

We measured CPU time of the computation of one-dimensional Betti numbers by Edelsbrunner-Lettsher-Zomorodyan algorithm (ELZ in the table) before

ICCS Camera Ready Version 2021
To cite this paper please use the final published version:
DOI: 10.1007/978-3-030-77961-0_32

and after reduction for both fragments. The time of the reduction was also measured. The results are shown in the table 5. The acceleration here is much higher than for the first series of tests. It is because the reduction algorithm does not remove voxels with neighbors with a higher filtration step, and these samples have only ten filtration steps, and they are quite large.

Figures 4, 5, 6 shows that the reduction does not preserve the geometry of the image. Preservation of geometry is not necessary, and it is enough to preserve topology.

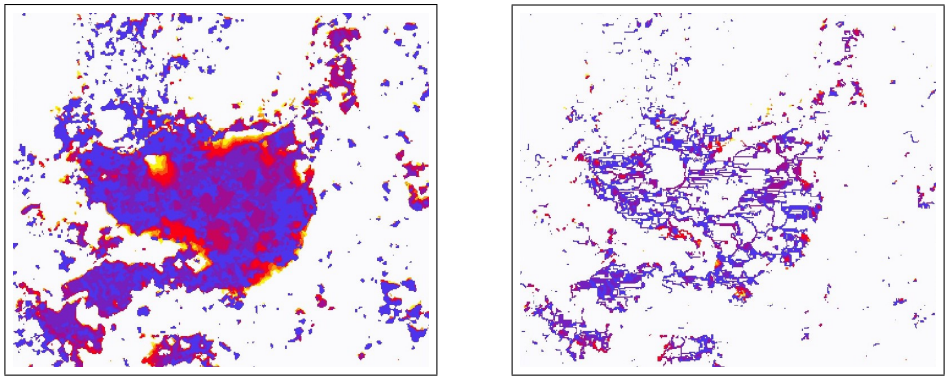

Fig. 4. Horizontal slices of the AH fragment before and after reduction. (Increase in the warmth of color corresponds to an increase in the filtration step.)

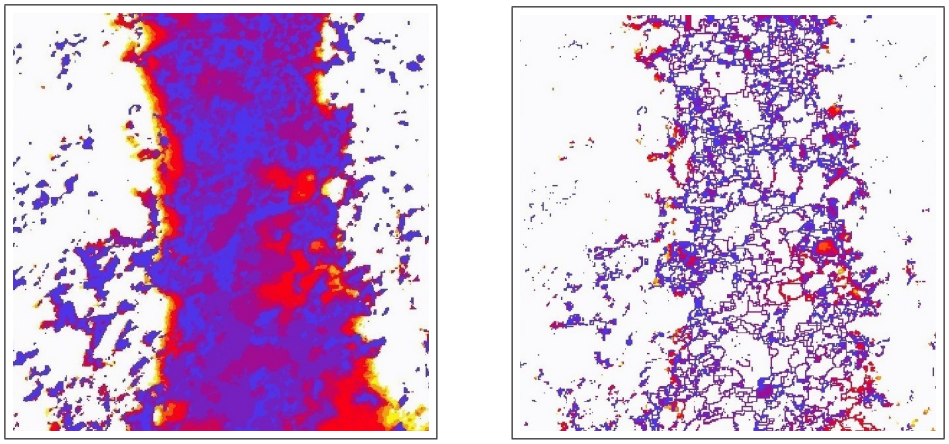

Fig. 5. Vertical slices of the AH fragment before and after reduction.

ICCS Camera Ready Version 2021
To cite this paper please use the final published version:
DOI: 10.1007/978-3-030-77961-0_32

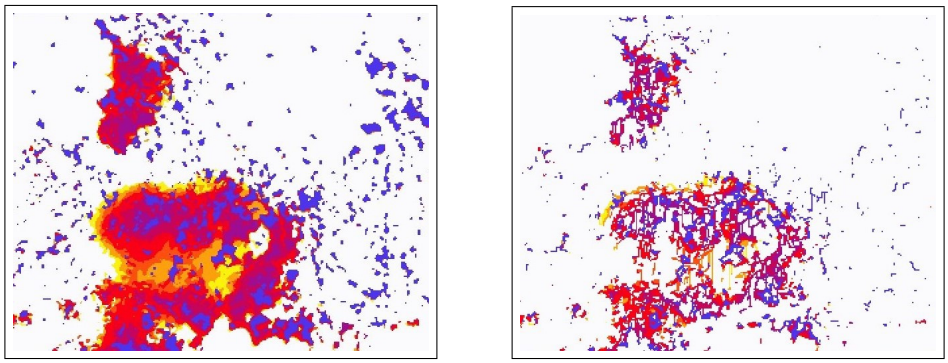

Fig. 6. Horizontal slices of the AL fragment before and after reduction.

6 Conclusion

The paper presents an algorithm for the reduction of a digital image of a porous medium. The algorithm is applicable to speed up the calculation of persistent Betty numbers, which are used to characterize the changes in the pore space's structure during the chemical dissolution of rock. It is shown that the use of the algorithm makes it possible to accelerate the calculation of persistent Betty numbers up to 70 times that leads to possibility of processing samples of sizes up to 500^3 voxels by using a single computational node within acceptable wall-clock time, that, less than 15 minutes (on the machine with Intel(R) Core(TM) i7-3770K CPU 3.5 GHz processor and 32 GB RAM installed, which was used for performed tests). Acceleration depends on the complexity of the pore space structure and the dynamics of the rock dissolution process.

The reduction algorithm allows parallelization. Thus, the first part of the future work is implementation and testing of parallel reduction. The second part is to study another methods of reducing input data for Edelsbrunner algorithm, such as co–reduction [20] and acyclic complex [7]. Then, we will be able to find the most efficient combination of reduction and these two methods for digital images of rock. It will allows us to quickly solve topological optimization problems in material design.

References

1. Al-Khulaifi, Y., Lin, Q., Blunt, M., Bijeljic, B.: Pore-scale dissolution by co2 saturated brine in a multi-mineral carbonate at reservoir conditions: Impact of physical and chemical heterogeneity (2019). https://doi.org/10.5285/52b08e7f-9fba-40a1-b0b5-dda9a3c83be2, http://dx.doi.org/10.5285/52b08e7f-9fba-40a1-b0b5-dda9a3c83be2
2. Al-Khulaifi, Y., Lin, Q., Blunt, M.J., Bijeljic, B.: Pore-scale dissolution by co2 saturated brine in a multimineral carbonate at reservoir conditions: Impact of physical and chemical heterogeneity. Water Resources Research **55**(4), 3171–3193 (2019)

ICCS Camera Ready Version 2021
To cite this paper please use the final published version:
DOI: 10.1007/978-3-030-77961-0_32

3. Alt-Epping, P., Waber, H.N., Diamond, L.W., Eichinger, L.: Reactive transport modeling of the geothermal system at bad blumau, austria: Implications of the combined extraction of heat and co2. Geothermics **45**, 18–30 (2013)
4. Amikiya, A.E., Banda, M.K.: Modelling and simulation of reactive transport phenomena. Journal of Computational Science **28**, 155–167 (2018)
5. Andra, H., Combaret, N., Dvorkin, J., Glatt, E., Han, J., Kabel, M., Keehm, Y., Krzikalla, F., Lee, M., Madonna, C., Marsh, M., Mukerji, T., Saenger, E.H., Sain, R., Saxena, N., Ricker, S., Wiegmann, A., Zhan, X.: Digital rock physics benchmarks - part i: Imaging and segmentation. Computers and Geosciences **50**(0), 25–32 (2013)
6. Bazaikin, Y., Gurevich, B., Iglauer, S., Khachkova, T., Kolyukhin, D., Lebedev, M., Lisitsa, V., Reshetova, G.: Effect of ct image size and resolution on the accuracy of rock property estimates. Journal of Geophysical Research: Solid Earth **122**(5), 3635–3647 (2017)
7. Dlotko, P., Wagner, H.: Simplification of complexes for persistent homology computations. Homology, Homotopy and Applications **16**, 49–63 (2014). https://doi.org/10.4310/HHA.2014.v16.n1.a3
8. Edelsbrunner, H., Harer, J.: Computational Topology, An Introduction. Amer. Math. Soc. (2010)
9. Gerke, K.M., Karsanina, M.V., Katsman, R.: Calculation of tensorial flow properties on pore level: Exploring the influence of boundary conditions on the permeability of three-dimensional stochastic reconstructions. Physical Review E **100**(5), 053312 (2019)
10. Hyman, J.D., Winter, C.L.: Stochastic generation of explicit pore structures by thresholding gaussian random fields. Journal of Computational Physics **277**, 16–31 (2014)
11. Jones, T.A., Detwiler, R.L.: Mineral precipitation in fractures: Using the level-set method to quantify the role of mineral heterogeneity on transport properties. Water Resources Research **55**(5), 4186–4206 (2019)
12. Kaya, E., Zarrouk, S.J.: Reinjection of greenhouse gases into geothermal reservoirs. International Journal of Greenhouse Gas Control **67**, 111–129 (2017)
13. Krahenbuhl, R.A., Martinez, C., Li, Y., Flanagan, G.: Time-lapse monitoring of co2 sequestration: A site investigation through integration of reservoir properties, seismic imaging, and borehole and surface gravity data. Geophysics **80**(2), WA15–WA24 (2015)
14. Lamy-Chappuis, B., Angus, D., Fisher, Q.J., Yardley, B.W.D.: The effect of co2-enriched brine injection on the mechanical properties of calcite-bearing sandstone. International Journal of Greenhouse Gas Control **52**(Supplement C), 84–95 (2016)
15. Lebedev, M., Zhang, Y., Sarmadivaleh, M., Barifcani, A., Al-Khdheeawi, E., Iglauer, S.: Carbon geosequestration in limestone: Pore-scale dissolution and geomechanical weakening. International Journal of Greenhouse Gas Control **66**, 106–119 (2017)
16. Lisitsa, V., Bazaikin, Y., Khachkova, T.: Computational topology-based characterization of pore space changes due to chemical dissolution of rocks. Applied Mathematical Modelling **88**, 21–37 (2020). https://doi.org/10.1016/j.apm.2020.06.037
17. Lucas, Y., Ngo, V.V., Clément, A., Fritz, B., Schäfer, G.: Modelling acid stimulation in the enhanced geothermal system of soultz-sous-forêts (alsace, france). Geothermics **85**, 101772 (2020)
18. Mokbel, D., Abels, H., Aland, S.: A phase-field model for fluid–structure interaction. Journal of Computational Physics **372**, 823–840 (2018)

ICCS Camera Ready Version 2021
To cite this paper please use the final published version:
DOI: 10.1007/978-3-030-77961-0_32

19. Mrozek, M., Batko, B.: Coreduction homology algorithm. Discrete and Computational Geometry **41**(1), 96–118 (2009)
20. Mrozek, M., Wanner, T.: Coreduction homology algorithm for inclusions and persistent homology. Computers and Mathematics with Applications **60**(10), 2812–2833 (2010)
21. Nestola, M.G.C., Becsek, B., Zolfaghari, H., Zulian, P., De Marinis, D., Krause, R., Obrist, D.: An immersed boundary method for fluid-structure interaction based on variational transfer. Journal of Computational Physics **398**, 108884 (2019)
22. Nooraiepour, M., Bohloli, B., Park, J., Sauvin, G., Skurtveit, E., Mondol, N.H.: Effect of brine-co2 fracture flow on velocity and electrical resistivity of naturally fractured tight sandstones. Geophysics **83**(1), WA37–WA48 (2018)
23. Pereira Nunes, J.P., Blunt, M.J., Bijeljic, B.: Pore-scale simulation of carbonate dissolution in micro-ct images. Journal of Geophysical Research: Solid Earth **121**(2), 558–576 (2016)
24. Saenger, E.H., Gold, N., Shapiro, S.A.: Modeling the propagation of the elastic waves using a modified finite-difference grid. Wave Motion **31**, 77–92 (2000)
25. Sim, C.Y., Adam, L.: Are changes in time-lapse seismic data due to fluid substitution or rock dissolution? a co2 sequestration feasibility study at the pohokura field, new zealand. Geophysical Prospecting **64**(4), 967–986 (2016)
26. Steefel, C.I., Appelo, C.A.J., Arora, B., Jacques, D., Kalbacher, T., Kolditz, O., Lagneau, V., Lichtner, P.C., Mayer, K.U., Meeussen, J.C.L., Molins, S., Moulton, D., Shao, H., Šimůnek, J., Spycher, N., Yabusaki, S.B., Yeh, G.T.: Reactive transport codes for subsurface environmental simulation. Computational Geosciences **19**(3), 445–478 (2015)
27. Trebotich, D., Adams, M.F., Molins, S., Steefel, C.I., Shen, C.: High-resolution simulation of pore-scale reactive transport processes associated with carbon sequestration. Computing in Science and Engineering **16**(6), 22–31 (2014)
28. Wagner, H., Chen, C., Vuçini, E.: Efficient Computation of Persistent Homology for Cubical Data, pp. 91–106. Springer Berlin Heidelberg, Berlin, Heidelberg (2012)
29. Wojtacki, K., Daridon, L., Monerie, Y.: Computing the elastic properties of sandstone submitted to progressive dissolution. International Journal of Rock Mechanics and Mining Sciences **95**, 16–25 (2017)

ICCS Camera Ready Version 2021
To cite this paper please use the final published version:
DOI: 10.1007/978-3-030-77961-0_32